

SCIENTIFIC REPORTS



OPEN

Elucidating the Performance Limitations of Lithium-ion Batteries due to Species and Charge Transport through Five Characteristic Parameters

Received: 07 June 2016

Accepted: 10 August 2016

Published: 07 September 2016

Fangming Jiang & Peng Peng

Underutilization due to performance limitations imposed by species and charge transports is one of the key issues that persist with various lithium-ion batteries. To elucidate the relevant mechanisms, two groups of characteristic parameters were proposed. The first group contains three characteristic time parameters, namely: (1) t_e , which characterizes the Li-ion transport rate in the electrolyte phase, (2) t_s , characterizing the lithium diffusion rate in the solid active materials, and (3) t_c , describing the local Li-ion depletion rate in electrolyte phase at the electrolyte/electrode interface due to electrochemical reactions. The second group contains two electric resistance parameters: R_e and R_s , which represent respectively, the equivalent ionic transport resistance and the effective electronic transport resistance in the electrode. Electrochemical modeling and simulations to the discharge process of LiCoO₂ cells reveal that: (1) if t_e , t_s and t_c are on the same order of magnitude, the species transports may not cause any performance limitations to the battery; (2) the underlying mechanisms of performance limitations due to thick electrode, high-rate operation, and large-sized active material particles as well as effects of charge transports are revealed. The findings may be used as quantitative guidelines in the development and design of more advanced Li-ion batteries.

Lithium-ion batteries have been widely applied in various portable consumer electronics. Compared with other batteries, lithium-ion batteries perform better in terms of energy-to-weight ratio, exhibit almost zero memory effect, and experience low self-discharge when in idle state^{1–4}. Nowadays, due to its very promising perspective for uses in electric vehicles (EV), smart grids and communication base stations, lithium-ion battery possibly grows into the dominant green energy storage or supply equipment of this century.

Main factors that retard the growth of lithium-ion battery include underutilization, stress-induced material damage, capacity fade, and possible occurrence of thermal runaway⁵. Researchers have poured considerable endeavors to commercialize different types and/or chemistries of lithium-ion batteries. Selecting a lithium-ion battery for a certain application depends mainly on the chemistry of cathode and other physical factors involved in the fabrication of cells, e.g. density of the material, composition and solid particle size in electrodes, and the cell geometry. Various chemistries have been considered for the fabrication of cathode materials for lithium-ion batteries^{6–11}. Several principal cathode materials are lithium cobalt oxide (LiCoO₂), lithium manganese oxide (LiMn₂O₄) and lithium iron phosphate (LiFePO₄). The Performance of the battery is significantly affected by the cell geometry, the cathode material and the preparation or fabrication method of cathode¹². Improving the design of batteries to realize maximum energy and power performance requires a thorough understanding of how physical properties of electrode materials such as species diffusivity and electric conductivity, operational parameters like charge/discharge rate, and cell structural parameters like electrode thickness and particle size of solid active materials influence the cell performance.

Laboratory of Advanced Energy Systems, Guangdong Key Laboratory of New and Renewable Energy Research and Development, CAS Key Laboratory of Renewable Energy, Guangzhou Institute of Energy Conversion, Chinese Academy of Sciences (CAS), Guangzhou 510640, China. Correspondence and requests for materials should be addressed to F.J. (email: fm_jiang2000@yahoo.com)

Extensive research has been conducted. Effects of electrode thickness^{13–16}, particle size^{17–21} and discharge rate^{22–26} on battery performance were quantified experimentally. Nagarajan *et al.*²⁷ established a mathematical model for the study of particle size distribution (PSD) effects on discharge behaviors of intercalation electrode systems. Results showed that the electrode utilization could be increased when using a binary mixture of differing particle sizes. Garcia *et al.*²⁸ developed a theoretical framework describing the kinetics of multiple charged species. The model results suggested controlling the transport paths to the back of the positive porous electrode, maximizing the surface area for intercalating lithium ions, and carefully controlling the spatial distribution and particle size of active materials could improve the battery performance. Golmon *et al.*²⁹ found from numerical simulations that electrodes with functionally graded porosity and particle size distribution could enhance the usable energy capacity of the battery. A detailed electrochemistry model coupled with an optimization algorithm was developed to examine^{30–34} the effects of cycling rate and cathode solid particle size, species diffusivity, and electronic conductivity on the specific energy and specific power of battery. It was found from simulation results that the available energy decreased with a faster cycling rate, larger active material particle size, and lower species diffusivity. Doyle *et al.*³⁵ found from experiments and simulations that minor solid-phase diffusion limitation effects existed in the carbon electrode and solution-phase diffusion limitations might become notably significant for a cell with an increased electrode thickness or a decreased initial salt concentration (decreased down to 1 mol•L⁻¹). A later work by Doyle *et al.*³⁶ derived analytical solutions, which described three performance-limiting phenomena due respectively to solution-phase diffusion, solid-phase diffusion, and charge transport. Arora *et al.*³⁷ concluded from experiments and simulations that the solution-phase diffusion limitations were the major limiting factor for Li-ion polymer cells during high-rate discharges. Smith *et al.*³⁸ found from numerical simulations that end of high-rate discharges might be caused by near-depletion of lithium species at negative electrode solid active material surfaces, full saturation of lithium at positive electrode solid active material surfaces, or local Li-ion depletion in the electrolyte. Hasan *et al.*³⁹ investigated the cell performance and the mechanisms limiting cell performance during fast-charge operations at moderate and extreme operation temperatures by an electrochemical-thermal coupling model. It was found that appropriate electrode design, such as a reduced electrode thickness and an increased porosity in the electrode, resulted in improved rapid-charge performance. Ogihara *et al.*⁴⁰ systematically investigated the dependence of the electrochemical behavior of intercalated LiNiO₂-based electrode on its thickness. They found that the ion-conduction pathway in the porous electrodes strongly affected the battery power capability; thick electrodes with high-loading active materials were found to have high energy density. Zhao *et al.*⁴¹ investigated the impacts of electrode thickness on the electrochemical and thermal properties of lithium-ion battery cells based on physical experiments and a combination model consisting of a one-dimensional (1D) electrochemical model and a three-dimensional (3D) thermal model. They found a battery of thicker electrodes had relatively higher internal resistance, which could result in a lower power output and an earlier stop of discharge (particularly high rate discharge) due to the longer diffusion distance and more serious concentration polarization.

A better understanding of the cell design and operational parameters on its overall performance can provide guidelines and benchmarks for tailoring battery design and constituting optimized management strategy for various application circumstances. Though a great amount of work has been done, there is still a lack of general and systematical analysis on the mechanisms of transport-related performance limitations of Li-ion batteries during charge/discharge operations. This work aims to elucidate the mechanisms of battery performance being limited by species and charge transport through a general characteristic analysis method. Five parameters are proposed to characterize the involved species and charge transport during battery charge/discharge processes, and how these parameters affect the battery performance is analyzed relying on a numerical model of Li-ion battery charge/discharge processes. Particularly, the numerical study takes the discharge process of a graphite/LiPF₆/LiCoO₂ battery to illustrate the characteristic analysis method; cases with different cell designs and/or operational parameters including electrode thickness, discharge rate, active material particle size, and material electric conductive property are calculated.

Characterizing Charge and Species Transport

Charge and species transport occur inside Li-ion batteries during discharge/charge processes. Charge transport includes ionic charge transport in the electrolyte and electronic charge transport in the solid phase; species transport includes Li-ion transport in the electrolyte and lithium transport in electrode active materials. These transport processes basically determine the performance of a Li-ion battery. For example, local Li-ion concentration in the electrolyte may be exhausted if the local consumption rate of Li-ions is far more than the transport rate of Li-ions in the electrolyte. And this phenomenon will lead to deteriorated performance (e.g. reduced capacity or capacity loss) of battery/cells. We characterize the species and charge transport in Li-ion battery charge/discharge processes to facilitate discussion about the mechanisms that limit the performance of Li-ion batteries.

Species transport in the electrolyte and solid phase. During Li-ion battery discharge/charge processes, the electrochemical reaction, which consumes or generates lithium atoms or ions (Li⁺), takes place at the interface of solid active materials and electrolyte; the lithium ions are being transported in the electrolyte by molecular diffusion and electric migration; the lithium atoms are diffusing into the solid active materials or out from the active material interior to the interface of solid and electrolyte phase. The governing equation for Li⁺ species transport in the electrolyte phase is formulated as⁴²:

$$\frac{\partial(\varepsilon_e c_e)}{\partial t} = \nabla \cdot D_e^{eff} \nabla c_e + \frac{1 - t_+^0}{F} j^{Li} \quad (1)$$

where D_e^{eff} denotes the effective diffusion coefficient of Li^+ in electrolyte phase, c_e is the lithium concentration in electrolyte, ε_e is the volume fraction of electrolyte, t is the time, t_+^0 is the transference number of Li^+ dissolved in the electrolyte, F is the Faraday's constant, and j^{Li} is the transfer current density. By assuming the solid active material to be some spherical particles, the equation governing lithium species transport in solid phase can be formulated as⁴²:

$$\frac{\partial c_s}{\partial t} = D_s \left(\frac{\partial^2 c_s}{\partial r^2} + \frac{2}{r} \frac{\partial c_s}{\partial r} \right) \quad (2)$$

where D_s denotes the diffusion coefficient of lithium in the solid active material, c_s is the lithium concentration in solid phase, and r is the spherical coordinate.

The transfer current density j^{Li} , which quantifies the electrochemical (EC) reaction rate, is normally calculated by the Butler-Volmer equation⁴²:

$$j^{Li} = a_s i_0 \left[\exp\left(\frac{\alpha_a F}{RT} \eta\right) - \exp\left(-\frac{\alpha_c F}{RT} \eta\right) \right] \quad (3)$$

where a_s denotes the specific surface area, i_0 is the exchange current density, α_a is the anodic transfer coefficient, α_c is the cathodic transfer coefficient, R is the universal gas constant, T is the temperature, and η is the surface overpotential.

We define three parameters to characterize the species transport processes in Li-ion batteries, i.e. t_e , t_s , and t_c .

$$t_e = \frac{L_{an}^2}{D_{e,an}^{eff}} + \frac{L_{sep}^2}{D_{e,sep}^{eff}} + \frac{L_{ca}^2}{D_{e,ca}^{eff}} \quad (4)$$

$$t_s = \frac{(r_0/3)^2}{D_s} \quad (5)$$

$$t_c = \frac{F \varepsilon c_e}{(1 - t_+^0) |j^{Li}|} \quad (6)$$

where, L_{an} , L_{ca} , and L_{sep} denote the thickness of anode electrode, cathode electrode and separator, respectively; r_0 represents the radius of the spherical active material particles. In Eq. (5), the factor 1/3 is the shape factor accounting for the diffusion transport in spherical objects⁴³. All the three parameters have the unit of time. Physically, t_e stands for a characteristic time describing the Li-ion transport rate in the electrolyte; t_s can be looked as a characteristic time characterizing the lithium diffusion process in the solid active materials; t_c is a characteristic time relating with the local Li-ion depletion rate in electrolyte at the electrolyte/electrode interface due to the EC reaction. Because of the presence of the transference coefficient (i.e. t_+^0) in Eq. (6), the effect of electric migration on Li-ion transport has been incorporated. We presume that there exists a relationship in-between these three parameters that can lead to the battery being of the best charge/discharge performance, without any performance-limitations due to species transport. Generally speaking, as long as the three characteristic time parameters are on the same order of magnitude, the battery should not get into any performance-limitations caused by the species transport processes.

Charge transport in the electrolyte and solid phase. The charge transport equation for lithium-ion charge in the electrolyte phase can be expressed as⁴²:

$$\nabla \cdot (\kappa^{eff} \nabla \varphi_e) + \nabla \cdot (\kappa_D^{eff} \nabla \ln c_e) + j^{Li} = 0 \quad (7)$$

where κ^{eff} denotes the effective ionic conductivity in electrolyte, and φ_e is the electric potential in electrolyte. By Taylor expansion with the second and higher order terms omitted with respect to the second term on the left-hand side of Eq. (7), it yields:

$$\nabla \cdot \left[\left(\kappa^{eff} + \kappa_D^{eff} \frac{1}{c_e} \frac{\partial c_e}{\partial \varphi_e} \right) \nabla \varphi_e \right] + j^{Li} = \nabla \cdot [\kappa^{eq} \nabla \varphi_e] + j^{Li} = 0 \quad (8)$$

The diffusional conductivity κ_D^{eff} is dependent on the ionic conductivity κ^{eff} , and can be calculated by virtue of concentrated solution theory⁴², as

$$\kappa_D^{eff} = \frac{2R\kappa^{eff}}{F} (t_+^0 - 1) \left(1 + \frac{d \ln f_{\pm}}{d \ln c_e} \right) \quad (9)$$

where f_{\pm} is the mean molar activity coefficient of the electrolyte.

Note that we have defined a parameter κ^{eq} in Eq. (8), which means the overall equivalent ionic conductivity in the electrolyte.

The electronic charge transport in solid phase is governed by the following conservation equation⁴²:

$$\nabla \cdot (\sigma^{eff} \nabla \varphi_s) - j^{Li} = 0 \quad (10)$$

where σ^{eff} denotes the effective electronic conductivity in solid phase, and φ_s is the electric potential in solid phase.

We define two parameters, namely, the equivalent ionic transport resistance in the electrolyte (i.e. R_e) and the effective electronic transport resistance in solid phase (i.e. R_s), to characterize the charge transport processes in electrodes.

$$R_e = \frac{L_{electrode}}{A_{electrode} \kappa^{eq}} \quad (11)$$

$$R_s = \frac{L_{electrode}}{A_{electrode} \sigma^{eff}} \quad (12)$$

where, $L_{electrode}$ (m) and $A_{electrode}$ (m²) represent the thickness and side surface area of the electrode, respectively. Note that $L_{electrode}$ may take different values for anode and cathode electrode. Physically, the charge transport will always seek transport paths of the least transport resistance, which may affect the electric potential (i.e. φ_s and φ_e) distributions and EC reaction distribution in the corresponding electrode.

Numerical modeling. Numerical modeling is widely used and plays an important role in the research and development of various electrochemical cells^{42,44–46}. In the present work, we choose the lithium cobalt oxide battery as a template Li-ion battery and establish a three-dimensional numerical model, which describes the electrochemical-physical processes in lithium cobalt oxide batteries during charge and discharge operations. For a lithium-ion battery of different chemistry, the involved multi-physical transport basically follows the same principles of conservation⁴⁷. Specially, we simulate discharge processes of lithium cobalt oxide batteries to study the performance limitations related to charge and species transport. We assume the battery is thermally well-managed and the whole battery remains at an optimum constant temperature (i.e. 25 °C considered in the present work) throughout the discharge process.

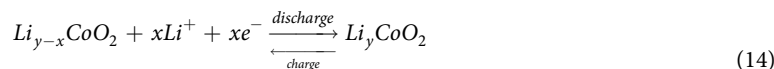
Physical and mathematical model. Figure 1 schematically shows the geometry and the involved species and charge transport during discharge of a graphite/LiPF₆/LiCoO₂ battery considered in the present work. The cell consists of a copper current collector (AC), a negative electrode, a separator, a positive electrode, and an aluminum current collector (CC). Both the electrodes and the separator are porous in nature. The electrode is composed of an active material, a polymer binder, some conductive filler, and the electrolyte. The active materials of anode and cathode are graphite mesocarbon microbeads and Li_yCoO₂, respectively. The electrolyte is lithium hexafluorophosphate (LiPF₆) in a mixture of propylene carbonate, ethylene carbonate, and dimethyl carbonate. The porous separator is composed of the liquid electrolyte and a polymer matrix. Illustrated also in Fig. 1 is the assumed lithium diffusion model in solid particles of anode and cathode active materials when discharging the battery.

During charge/discharge processes, the EC reactions occurring in electrodes can be expressed as follows.

In the anode composite electrode,



In the cathode composite electrode,



The electrochemical model for graphite/LiPF₆/LiCoO₂ battery developed in this work is based on porous electrode and concentrated solution theories^{48,49}. Major assumptions include⁴² (1) Electrode active materials are assumed to be spherical particles of uniform size; (2) Side reactions are ignored and no gas phase is present during charge/discharge operations; (3) The electrolyte is a concentrated binary solution, which means that it is dissociated into a cation and an anion; (4) The transport of lithium species relies on diffusion and migration in the electrolyte solution while only on diffusion in the solid active materials; (5) EC reactions of lithium insertion and extraction processes follow the Butler-Volmer equation, i.e. Eq. (3), which describes a large class of electrode reactions; (6) Interfacial electrical and chemical equilibrium exist at the electrode/electrolyte interface; (7) The effective transport coefficients are calculated in terms of the Bruggeman theorem⁵⁰, namely, $\pi^{eff} = \pi \varepsilon^{1.5}$, where π denote the intrinsic transport coefficient of a material and ε the component volume fraction of this material in the composite electrodes/separator.

In numerical modeling, we treat the battery as a single-domain of multiple sub-regions associated with different sets of physical-chemical properties. This circumvents difficulties about matching boundary conditions at the interior interfaces of the battery. The model equations together with boundary conditions for battery discharge process are summarized in Table 1⁴². The governing equations, Eqs (1), (7) and (10), describe the macroscopic transport in the cell; Eq. (2) describes the microscopic diffusion of lithium in solid active material particles, as illustrated in Fig. 1. The combined micro/macroscopic model is essential to model the transport processes during

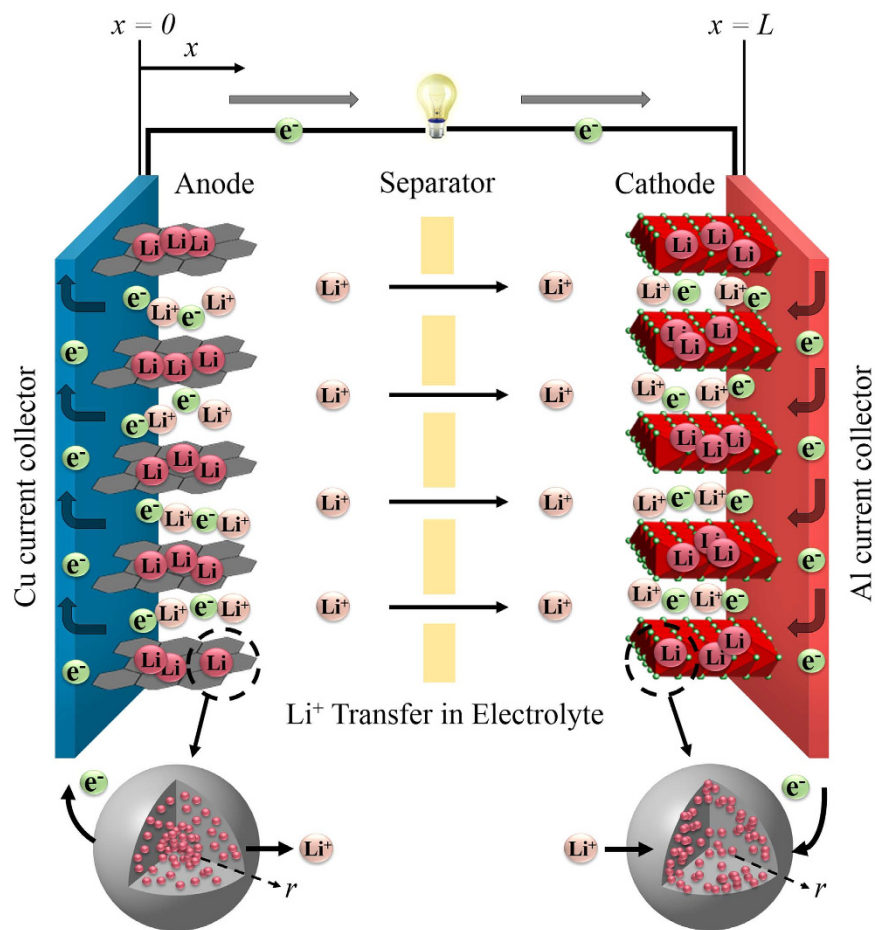


Figure 1. Schematic of the involved species/charge transports and electrochemical reactions in lithium-ion cells during discharge. The electrode through-plane direction is indicated by the x coordinate.

	Conservation equations	Boundary conditions
Species, electrolyte phase	$\frac{\partial c_s}{\partial t} = \nabla \cdot D_e^{eff} \nabla c_e + \frac{1-t_+^0}{F} j^{Li}$ (1)	$\frac{\partial c_e}{\partial x} \Big _{x=0} = \frac{\partial c_e}{\partial x} \Big _{x=L} = 0$; Zero flux at other boundaries
Species, solid phase	$\frac{\partial c_s}{\partial t} = D_s \left(\frac{\partial^2 c_s}{\partial r^2} + \frac{2}{r} \frac{\partial c_s}{\partial r} \right)$ (2)	$\frac{\partial c_s}{\partial r} \Big _{r=0} = 0$; $j^{Li}(t) = -a_s F D_s \frac{\partial c_s}{\partial r} \Big _{r=r_0}$
Charge, electrolyte phase	$\nabla \cdot (\kappa_e^{eff} \nabla \varphi_e) + \nabla \cdot (\kappa_D^{eff} \nabla \ln c_e) + j^{Li} = 0$ (7)	$\frac{\partial \varphi_e}{\partial x} \Big _{x=0} = \frac{\partial \varphi_e}{\partial x} \Big _{x=L} = 0$; Zero flux at other boundaries
Charge, solid phase	$\nabla \cdot (\sigma^{eff} \nabla \varphi_s) - j^{Li} = 0$ (10)	$-\sigma \frac{\partial \varphi_s}{\partial x} \Big _{x=0} = -\sigma \frac{\partial \varphi_s}{\partial x} \Big _{x=L} = \frac{I}{A}$; Zero flux at other boundaries

Table 1. Governing equations and boundary conditions (for discharge) for the cases considered.

lithium ion battery charge/discharge operations. Table 2 presents the values of major parameters used in the present study.

Numerical strategy. Once appropriate boundary conditions are defined, as shown in Table 1, and initial conditions are established, the governing equation group consisting of Eqs (1), (2), (7) and (10) is solved for the four unknowns: φ_s , φ_e , c_e , and c_s ($c_{s,e} = c_s|_{r=R_s}$) in the commercial computational fluid dynamics flow solver, Fluent[®], which is based on the finite volume approximation. By customizing its User Defined Functions, various source terms and physicochemical properties are implemented. The first order upwind differencing scheme is generally used to discretize the spatial-derivative terms and a fully implicit scheme is used to discretize the transient terms. To accelerate convergence, the algebraic multi-grid iterative method is applied to solve the linearized algebraic equations. A flow chart is presented in Fig. 2 to illustrate the overall procedure of the Fluent[®] computational program.

Parameters	Cu current collector	Anode	Separator	Cathode	Al current collector
Thickness ^a (Base case), L (μm)	10	80	25	64	10
Particle radius ^a (Base case), r ₀ (μm)		10	N/A	8	
Porosity ^a , ε		0.35	0.42	0.3	
Specific area in electrode ^a (Base case), a _s (m ² m ⁻³)		1.79E5		2.35E6	
Maximum Li ⁺ concentration in solid ^a (mol m ⁻³)		28555	N/A	51555	
Initial electrolyte concentration ^a , c _e (mol m ⁻³)		1000			
Reference exchange current density ⁵⁶ , i ₀ (A m ⁻²)		36		26	
Solid phase electronic conductivity, σ (S m ⁻¹)	6.0E7 ⁵⁷	100.0 ⁵⁶	0	10 ⁵⁶	3.8E7 ⁵⁶
Ionic conductivity in electrolyte ^a , κ (S m ⁻¹)	0	Eq. (16)			
Li ⁺ diffusion coefficient in electrolyte ⁵⁸ , D _e (m ² s ⁻¹)	0	$D_e = 10^{-4.43 - 54.0/(T - 229 - 5c_e) - 0.22c_e}$			
Li diffusion coefficient in solid, D _s (m ² s ⁻¹)		$D_s = 3.9 \times 10^{-14} (1.5 - \text{SOC})^{3.5 59}$	N/A	1.0E-13 ⁵⁶	
Surface overpotential, η (V)		$\eta = \phi_s - \phi_e - U$			
Open circuit voltage, U (V) ⁵⁶		Eq. (17)		Eq. (18)	
mean molar activity coefficient of the electrolyte, f _± ⁶⁰		1			
Anodic/Cathodic transfer coefficient ⁵⁶ , α _a , α _c		0.5		0.5	
Transference number ⁵⁶ , t ₊ ⁰		0.363			
Faraday's constant, F (C mol ⁻¹)		96487.0			

Table 2. Model parameters. ^aData from our industrial partner: Amperex Technology Limited.

To examine the error of numerical discretization, the Richardson extrapolation technique⁵¹ was adopted. The obtained result indicates all the calculated values of the major variables deviate from the corresponding extrapolated accurate values by about 5% at most for the numerical mesh system used in the present work, approving the accuracy and fidelity of the simulation results.

The above-described electrochemical model is actually an adaption of a previous model⁴², which modeled LiFePO₄/graphite batteries and was validated by comparing the simulated cell voltage curves with and the experimentally measured ones during battery discharge processes. Therefore, an experimental validation of the present model was omitted.

Cases considered. We consider six cases to study the mechanisms for species and charge transport limit the performance of Li-ion batteries. The base case (i.e. case 1) has realistic battery design and is operated at normal discharge rate, 1C; the electric conductivities (κ and σ both) are specified with real values. Cases 2–4 differs from the base case due to thicker electrode design, larger size of active material particles, or being operated at a higher discharge rate. Cases 5 and 6 have an artificially-reduced electric conductivity by a reduction factor of 10 and 100, respectively. In reality, a reduced electric conductivity may be found in electrodes of decreased carbon contents or different doping strategies^{52–55}. Main parameters of the six cases considered are summarized in Table 3.

In terms of the definition of the five parameters, i.e. Eqs (4), (5), (6), (11) and (12), we calculate their values and tabulate in Table 4. For the base case, t_e, t_s, and t_c are approximately on the same order of magnitude except the t_s in the anode, which is obviously larger than the t_e and t_c; for cases 2–4, the value of one of the three characteristic times is much longer than the other two. In cases 5 and 6, the magnitudes of R_c-s are artificially enlarged by a factor of 10 and 100, respectively, compared with case 1. It is worth pointing out that the magnitude of transfer current density (i.e. |j^{Li}|) was approximated by assuming uniform EC reactions in electrodes when calculating the values of t_c tabulated in Table 4, namely,

$$|j^{Li}| \approx \frac{I}{AL_{electrode}}, \quad (15)$$

where I denotes the imposed current load and A the side surface area of the current collector plate.

$$\begin{aligned} \kappa = & 20.8409 \frac{c_e}{1000} - 21.29 \left(\frac{c_e}{1000} \right)^2 + 13.6986 \left(\frac{c_e}{1000} \right)^3 \\ & - 7.58544 \left(\frac{c_e}{1000} \right)^4 + 2.45464 \left(\frac{c_e}{1000} \right)^5 - 0.30446 \left(\frac{c_e}{1000} \right)^6 \end{aligned} \quad (16)$$

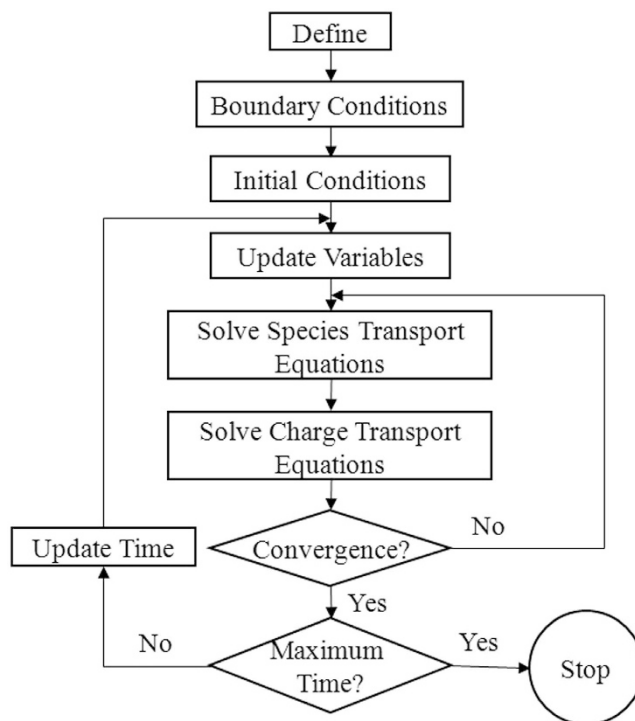


Figure 2. Flow chart of the computational program.

Case #	Thickness (μm)		Particle size (μm)		Electric conductivity in electrodes	Discharge rate
	Anode	Cathode	Anode	Cathode		
Case 1 (Base case)	80	64	10	8	κ, σ	1C
Case 2	400	320	10	8	κ, σ	1C
Case 3	80	64	10	8	κ, σ	10C
Case 4	80	64	40	32	κ, σ	1C
Case 5	80	64	10	8	$\kappa, \sigma/10$	1C
Case 6	80	64	10	8	$\kappa, \sigma/100$	1C

Table 3. Simulated cases.

Case #	t_c (s)	t_s (s)		t_c (s) ^{c1}		R_c (Ω) ⁻²		R_s (Ω) ^{c2}	
		Anode	Cathode	Anode	Cathode	Anode	Cathode	Anode	Cathode
Case 1	180.4	3.2E3	71.1	147.7	101.3	4.9E-5	4.9E-5	1.7E-6	1.0E-5
Case 2	4.4E3	3.2E3	71.1	147.7	101.3	2.5E-4	2.5E-4	8.2E-6	5.0E-5
Case 3	180.4	3.2E3	71.1	14.8	10.1	4.9E-5	4.9E-5	1.7E-6	1.0E-5
Case 4	180.4	5.2E4	1.1E3	147.7	101.3	4.9E-5	4.9E-5	1.7E-6	1.0E-5
Case 5	180.4	3.2E3	71.1	147.7	101.3	4.9E-5	4.9E-5	1.7E-5	1.0E-4
Case 6	180.4	3.2E3	71.1	147.7	101.3	4.9E-5	4.9E-5	1.7E-4	1.0E-3

Table 4. Values of the five characteristic parameters when the battery is in the idle state prior to discharge. ^{c1} $|j^{Li}|$ is calculated by Eq. (15). ^{c2}The side surface area of electrodes takes the value of 1 m^2 .

$$\begin{aligned}
 U_{anode} = & 0.13966 + 0.68920 \exp(-49.20361SOC) \\
 & + 0.41903 \exp(-254.40067SOC) \\
 & - \exp(49.97886SOC - 43.37888) \\
 & - 0.028221 \arctan(22.523SOC - 3.65328) \\
 & - 0.01308 \arctan(28.34801SOC - 13.43960)
 \end{aligned} \tag{17}$$

$$\begin{aligned}
 U_{cathode} = & 4.04596 + \exp(-42.30027DOD + 16.56714) \\
 & - 0.0488 \arctan(50.01833DOD - 26.48897) \\
 & - 0.05447 \arctan(18.99678DOD - 12.32362) \\
 & - \exp(78.240895DOD - 78.68074)
 \end{aligned} \tag{18}$$

Simulated Results and Discussion

Base case (Case 1). The simulated spatial distribution of Li-ion concentration (c_e) in the electrolyte and its temporal change for the base case (i.e. case 1) are depicted in Fig. 3(a). A distribution of Li-ion concentration quickly builds up inside the cell upon discharge, forming a gradient which drives Li-ion species transport along the cell thickness direction from the anode to cathode. A maximum of $1150 \text{ mol}\cdot\text{m}^{-3}$ Li-ion concentration is calculated in the anode at 450 s and a minimum of $830 \text{ mol}\cdot\text{m}^{-3}$ Li-ion concentration is calculated in the cathode at 3595 s. Except for the very early period of the discharge process, during which the c_e evidently increases in the anode and decreases in the cathode with time, the distribution of c_e shows small variations with time. For the base case, t_e is larger than t_c as shown in Table 4, which means the consumed Li-ion in the cathode or the generated Li-ion in the anode due to local EC reactions can be supplemented or removed by the Li-ion transport process in the electrolyte. That is to say, the Li-ion transport in electrolyte does not impose any limitation to the cell discharge performance.

The time-variation of the spatial distribution of state of discharge (SOC) in the anode and depth of discharge (DOD) in the cathode for the base case are shown in Fig. 3(b). The SOC in anode and DOD in cathode are defined as

$$SOC, DOD = \frac{c_{s,e} - c_{s,\min}}{c_{s,\max} - c_{s,\min}} \tag{19}$$

where $c_{s,e}$ is the lithium concentration at the surface of solid active material particles; $c_{s,\max}$ and $c_{s,\min}$ are the allowed maximum and minimum concentration of lithium in the solid active material, respectively.

Seen from Fig. 3(b), the SOC decreases and the DOD increases with time as expected. Along the cell thickness direction the DOD in the cathode shows relatively more uniform distribution than the SOC in the anode; the minimum SOC appears in the near-region of the electrode/separator interface in the anode. The discharge process lasts for about 1 hour, the SOC in anode decreases from 1 to 0 and the DOD in cathode increases from 0 to 1, indicating no detectable performance limitation for the cell discharge process.

Figure 3(c) gives the spatial distribution and temporal change of the electrolyte phase potential (φ_e) in the base case. It decreases overall with time throughout the discharge process and specifically during the late period of the process, the decrease is at a much faster rate. This is due to the diminishing open circuit potentials. Across the direction of the cell thickness, the magnitude of φ_e value decreases with an increase in x value, forming a φ_e gradient to drive Li-ion charge transport from the anode to cathode.

Figure 3(d) shows the spatial distribution and temporal change of the solid phase potential (φ_s) of the base case. In the cathode, the φ_s value decreases overall with time throughout the discharge process; during the late period of the process, the φ_s is seen to decrease a lot. The value of φ_s in the anode overall changes little with time as a φ_s reference point (-3.02 V) is set in the anode current collector. In the anode across the cell thickness direction, the φ_s value slightly decreases with the increase of x and in the cathode it also slightly decreases with the increase of x , forming φ_s gradients to drive electronic charge transport from the separator side to the current collector side in the anode and from the current collector side to the separator side in the cathode. The overall decrease of φ_s value in the cathode is due to the decreasing open circuit potential.

D_s is a constant value for cathode whereas in anode it is time variant; the D_e is a function of the c_e . (See in Table 2) Fig. 3(e,f) give the time-variation history of D_s in the anode and D_e in the electrolyte, respectively. The D_s in anode increases with time, from 5.0×10^{-15} to $1.5 \times 10^{-13} \text{ m}^2 \text{ s}^{-1}$, substantially improving the lithium diffusion in solid active materials; the D_e shows relatively smaller spatial and temporal changes, within $2.9\text{--}3.6 \times 10^{-10} \text{ m}^2 \text{ s}^{-1}$. Along the cell thickness direction D_s in the anode shows relatively uniform distribution. Except for the very early period of the discharge process, during which the D_e evidently decreases in the anode and increases in the cathode with time, the distribution of D_e changes little with time. The value of D_e in the cathode is larger than that in the anode.

Figure 3(g) gives the time-variation history of κ^{eq} . The κ^{eq} shows little temporal dependence, but relatively larger spatial dependence, and in the separator it takes the maximum value. The ionic conductivity κ , which is a function of c_e (refer to Eq. (16)), takes a maximum value when $c_e = 1.0 \text{ mol}\cdot\text{L}^{-1}$. From Fig. 3(a), though there is a c_e distribution quickly forming in the cell upon discharge, the c_e value in the separator region is around $1.0 \text{ mol}\cdot\text{L}^{-1}$ all the time through the discharge process. This adequately explains the spatial dependence of κ^{eq} and why the κ^{eq} is seen to take the maximum value in the separator region.

Figure 3(h) gives the spatial and temporal evolution of j^{Li} , the magnitude of which reflects the electro-chemical reaction intensity. Upon discharge, the EC reactions occur and a transfer current density distribution quickly builds up in both the electrodes. In the anode, the transfer current density is positive while in the cathode is negative. Overall, the EC reaction in the cathode is more uniform than that in the anode. In the anode, the transfer current density fluctuates with time and the location with stronger EC reaction shifts frequently. In the cathode, the near-region of separator is seen to have slightly stronger EC reaction for most time of the discharge process, though some small fluctuations at the location of stronger EC reaction are also seen; in the late period of the discharge process, after $\sim 3500 \text{ s}$, the near-region of cathode current collector has distinctly stronger EC reaction.

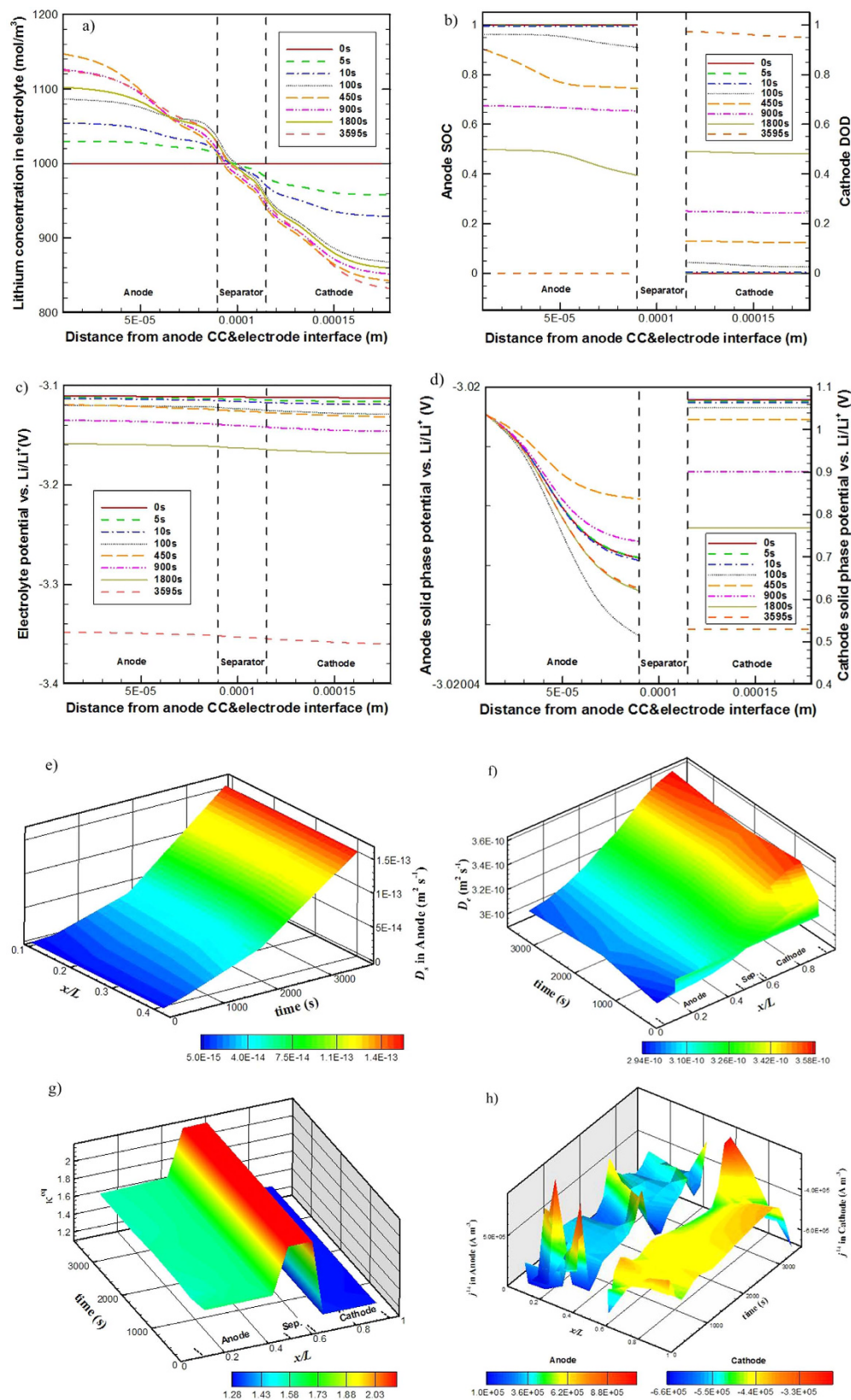


Figure 3. Detailed simulation results from the base case: time-variation of Li^+ concentration distribution in electrolyte (a), of SOC in anode and DOD in cathode (b), of electrolyte phase potential distribution (c), and of solid phase potential distribution (d); spatial and temporal evolution of D_s at the surface of anode active material particles (e), of D_e in the electrolyte (f), of κ^{eq} (g), and of j^{Li} (h).

Time instant (s)	t_e (s)	t_s (s)		t_c (s)		R_e (Ω) ^{c2}		R_s (Ω) ^{c2}	
		Anode	Cathode	Anode	Cathode	Anode	Cathode	Anode	Cathode
10	178.3–182.0	3.1E3–3.1E3	71.1	122.0–184.0	69.6–124.3	4.9E-5	4.9E-5–5.0E-5	1.7E-6	1.0E-5
100	177.0–183.2	1.8E3–2.5E3		53.6–618.8	80.0–103.2	4.9E-5–5.0E-5	5.0E-5		
500	174.0–187.5	7.5E2–1.2E3		66.7–351.4	80.4–101.0	4.9E-5–5.0E-5	5.0E-5		
1000	175.2–185.2	4.7E2–5.0E2		158.4–163.1	87.8–91.9	4.9E-5–5.0E-5	5.0E-5		
1800	176.2–184.1	2.0E2–2.8E2		79.2–257.4	89.7–91.0	4.9E-5–5.0E-5	5.0E-5		
2400	174.5–186.3	1.5E2–1.7E2		103.5–296.4	83.5–93.2	4.9E-5–5.0E-5	5.0E-5		
3595	174.9–185.4	68.9–69.0		83.1–262.1	56.9–174.3	4.9E-5–5.0E-5	5.0E-5		

Table 5. Time-variation of the five characteristic parameters during discharge for the base case. ^{c2}The side surface area of electrode takes the value of 1 m².

Table 5 summarizes the time-variation of the five characteristic parameters. During the discharge process, the variation of t_e is small due to the small spatial and temporal changes of the D_e . (Refer to Fig. 3(f)). The t_s in anode remarkably decreases with time due to the substantial increase of D_s during the discharge process. (See Fig. 3(e)) The spatial and temporal changes of j^{Li} and c_e (See Fig. 3(a,h)) leads to the time-variation of t_c , which are not large for this particular case. In the early period of the discharge process the t_s in the anode is obviously larger than the t_e and t_c . However, the diffusion of lithium in the anode active material particles should occur only in the particle's near-surface region during the early period of discharge; calculating the t_s in terms of the characteristic size parameter r_0 overestimates the real characteristic time for the lithium diffusion in anode active material particles. The t_s in the anode is largely reduced with the progress of discharge; after about 1000 s discharge, the t_s in the anode turns to be on the same order of magnitude of the t_e and t_c . Therefore, the cell is fully discharged without any capacity loss.

Seen from Table 5 also, the R_s is constant and the R_e shows small changes with time due to the spatial and temporal changes of κ^{eq} (see Fig. 3(g)). Detailed discussion about the charge transport effects on the cell performance will be presented in Section 4.5.

Thick electrode case (Case 2). Increasing the thickness of electrodes might be an effective way to simultaneously enhance the energy density and power density both of Li-ion batteries⁴⁰. Case 2 considers a cell, in which the electrode thickness is five times of the base case for both anode and cathode side. The simulated spatial distribution and temporal change of SOC in the anode and DOD in the cathode for case 2 are shown in Fig. 4(a). The SOC decreases and the DOD increases with time during the discharge process. The SOC in anode and the DOD in cathode both show very large non-uniform profiles. The discharge process terminates at about 365 s, which is far below the 1C discharge time, 3600 s. The t_e is approximately proportional to the square of electrode thickness. (See Eq. (4)) The 4-times increased electrode thickness of case 2 largely increases the value of t_e (see in Table 4), which causes severe capacity loss, only about 10% of the stored electricity can be discharged; a large portion of the electrodes is actually not in use.

Figure 4(b) shows the spatial distribution and temporal change of Li-ion concentration (c_e) in electrolyte for case 2. The c_e value increases in the anode and decreases in the cathode throughout the discharge process. A maximum of 2100 mol·m⁻³ Li-ion concentration is calculated in the anode and a minimum of 0 mol·m⁻³ Li-ion concentration is calculated in the cathode at the end of discharge process. The zero c_e in the near-region of the cathode current collector indicates that the lithium ion is depleted in the electrolyte, which is due mainly to the too slow Li-ion transport speed (i.e. too large t_e) in the electrolyte.

From Table 2, for case 2 it is clearly shown that the t_e is much larger than the t_c -s, which means in the electrolyte the Li-ion consumption/generation speed due to local EC reactions in the cathode/anode cannot be supplemented/removed in time by the Li-ion transport in the electrolyte phase. Therefore, we see in Fig. 4(b) very large value of c_e and locally zero c_e value present in the anode and cathode, respectively.

Figure 4(c) gives the spatial distribution and temporal change of the electrolyte phase potential (φ_e) for case 2. The φ_e value overall decreases with time throughout the discharge process. A zero φ_e gradient appears in the near-regions of the two current collectors, indicating actually no ionic charge transport presents in these regions.

Figure 4(d) presents the time-variation history of D_e distribution in the electrolyte for case 2. D_e value decreases in anode and increases in cathode with time. For case 2, the distribution of D_e shows larger spatial and temporal dependence than the base case as the c_e distribution for case 2 tends to establish larger gradients across the separator along the electrode through-plane direction (refer to Figs 3(a) and 4(b)).

Figure 4(e) gives the time-variation history of the κ^{eq} distribution in the electrolyte phase for case 2. The κ^{eq} result for case 2 shows larger spatial and temporal changes compared with the result of the base case given in Fig. 3(g). Due to the resultant zero c_e in cathode, the κ^{eq} for case 2 even shows very low (close to zero) κ^{eq} in the near-region of the cathode current collector during the late period of the discharge process. This leads to a very large ionic charge transport resistance, making the discharge operation actually not viable in this region.

Table 6 summarizes the time-variation of the t_e , t_s , and t_c for case 2. The t_e and t_c -s all show larger amounts of changes than those for the base case (see Table 5), whereas the t_s in anode shows smaller amounts of increase due to the incomplete Li-insertion process. For case 2 itself, the time-variation of t_e is not that significant as that of t_c in cathode, and the t_e remains always much larger than the t_s in cathode and the t_c -s. The largely reduced c_e and the locally increased transfer current density in the cathode owing to partially cease-operation of the cell dramatically

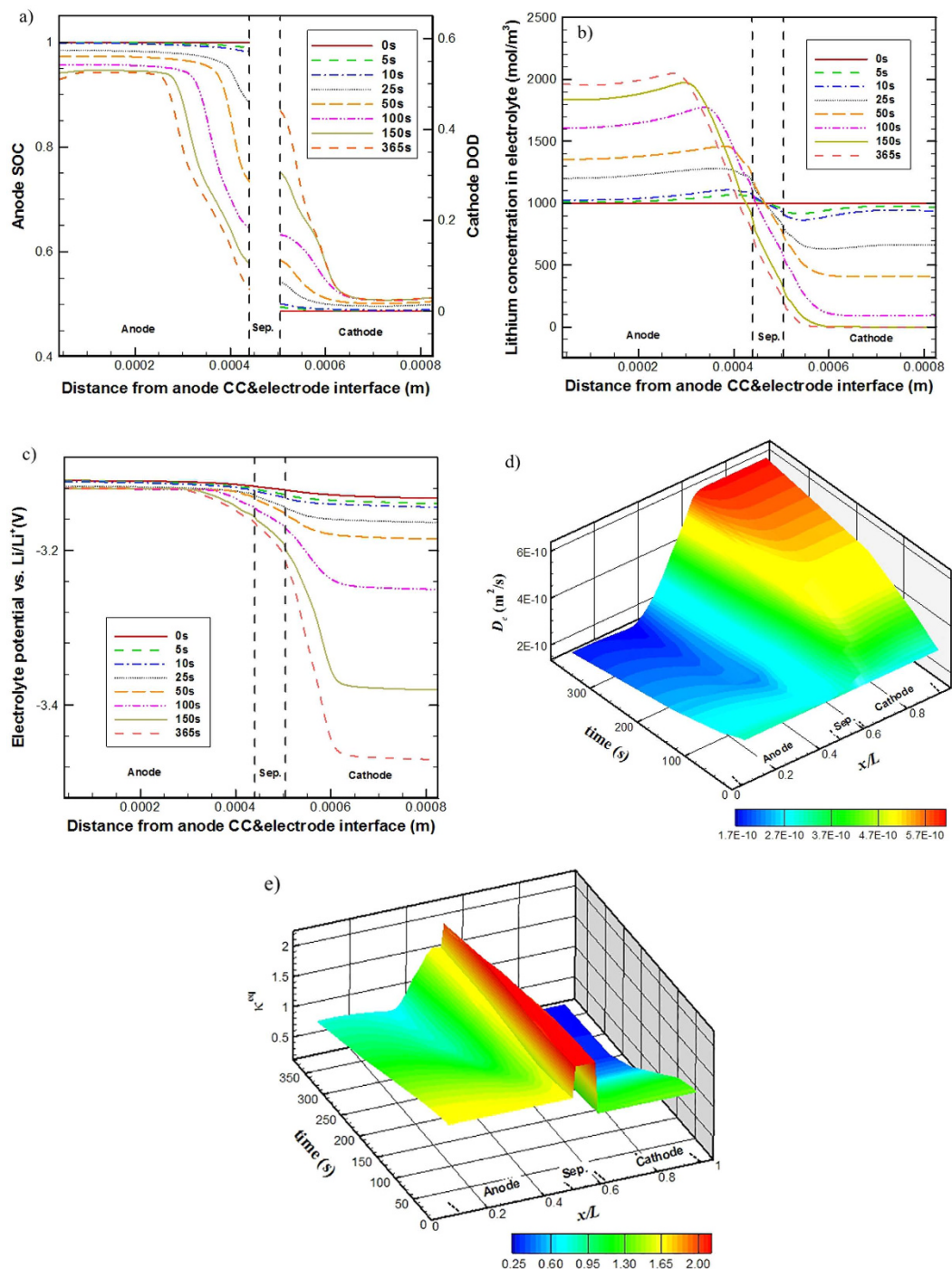


Figure 4. Part of simulation results from case 2: time-variation of SOC in anode and DOD in cathode (a), of Li⁺ concentration distribution in electrolyte (b), and of electrolyte phase potential distribution (c); spatial and temporal evolution of D_c in the electrolyte (d), and of κ^{eq} (e).

shorten the value of the t_c in cathode, which combines the too slow Li-ion transport speed to lead to a quick termination of the discharge process.

High rate discharge case (Case 3). The practical uses of various lithium-ion batteries of different capacities often require the batteries being of adequate high-rate charge/discharge capability²⁴. Case 3 considers a 10C discharge process. The simulated spatial distribution and temporal change of SOC in the anode and DOD in the cathode are depicted in Fig. 5(a). The SOC decreases and the DOD increases with time during the discharge process. The SOC in anode and the DOD in cathode both show very large non-uniform profiles. The discharge process terminates at about 185 s, which is about half of the 10C discharge time, meaning only about 50% of the

Time instant (s)	t_e (s)	t_s (s)		t_c (s)	
		Anode	Cathode	Anode	Cathode
5	4.3E3–4.5E3	3.0E3–3.2E3	71.1	52.3–388.9	28.9–195.5
10	4.3E3–4.5E3	2.9E3–3.2E3		57.5–283.4	27.8–163.5
50	4.3E3–4.6E3	1.6E3–2.9E3		25.3–372.3	22.0–123.1
100	4.2E3–4.9E3	724.2–2.7E3		37.5–560.2	19.4–108.5
180	3.9E3–5.4E3	522.7–2.5E3		55.5–778.8	7.9–56.1
240	3.6E3–5.7E3	445.6–2.3E3		72.1–1.0E3	1.7–21.6
365	3.2E3–6.0E3	315.3–2.2E3		39.8–3.0E3	0.4–30.7

Table 6. Time-variation of the t_e , t_s , and t_c during discharge for case 2.

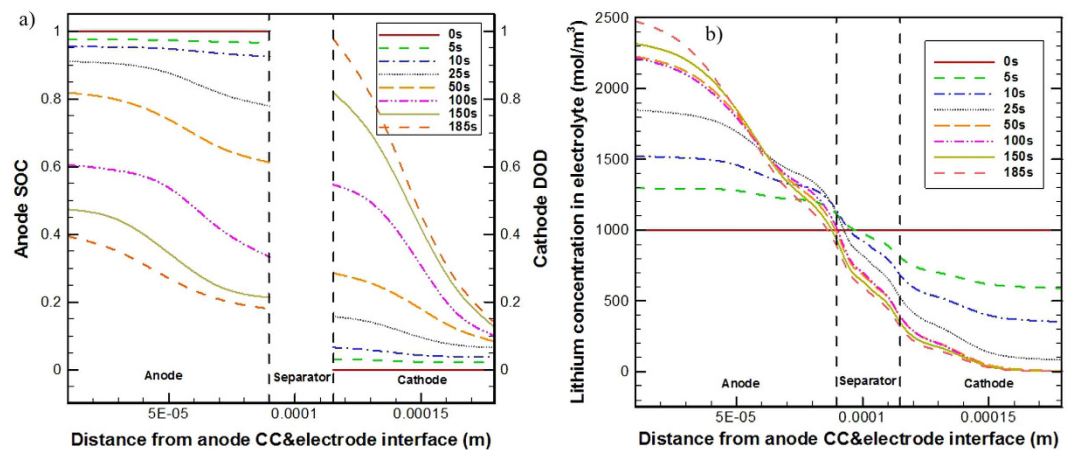


Figure 5. Time-variation of SOC in anode and DOD in cathode (a), and of Li^+ concentration distribution in electrolyte (b) for case 3.

stored electricity is discharged. The t_c is inversely proportional to the discharge current. The 10-times increased current load greatly shortens the value of t_c (see in Table 4), leading to too fast speed of Li-ion consumption/generation owing to the EC reactions in the cathode and anode, respectively.

Figure 5(b) gives the spatial distribution and temporal change of Li-ion concentration (c_e) in the electrolyte for case 3. The c_e increases overall in the anode and decreases in the cathode with time. The large current density renders a c_e profile of large difference along the electrode through-plane direction. A maximum of $2500 \text{ mol}\cdot\text{m}^{-3}$ Li-ion concentration is calculated in the anode and a minimum of $0 \text{ mol}\cdot\text{m}^{-3}$ Li-ion concentration is calculated in the cathode at the end of discharge process. The zero value of c_e in the near-region of the cathode current collector indicates that the Li-ion in the electrolyte is depleted. The discharge process terminates at 185 s, much less than the 10 C discharge time, 360 s, signifying again severe capacity loss.

Table 7 summarizes the time-variation of the t_e , t_s , and t_c . Compared with the base case (see Table 5), the t_e and t_c for case 3 both show larger amount of changes, whereas the t_s in anode shows smaller amount of changes due to the incomplete Li-insertion process. For case 3 itself, the t_c -s remain always much smaller than the t_s in anode and the t_s ; the time-variation of t_c in the cathode is very significant, it is shortened dramatically due to the largely reduced c_e , exacerbating the performance-limitation condition and finally leading to a quick termination of the discharge process.

It has been shown previously³⁷ that high-rate discharges of Li-ion batteries are limited by species transport processes, which can be the Li-ion species transport in the electrolyte phase or the lithium transport in the solid active material phase or the both. However, it is still not clear which factor is the main limitation mechanism to the high-rate discharges of Li-ion batteries. From the above-detailed analysis of case 3 in the present work, the performance limitations of high-rate charge/discharge processes are essentially due to the very short t_e , i.e. the too fast depletion of Li-ions in electrolyte phase due to the EC reaction.

Case with active materials of larger particle size (Case 4). Case 4 considers active material particles of larger sizes, in anode and cathode both the active material particle size is increased by a factor of 4. As the t_s is directly proportional to the squared particle radius, it is 25-times enlarged. The simulated spatial distribution and temporal change of SOC in the anode and DOD in the cathode for case 4 are presented in Fig. 6(a). The SOC in anode is reduced down to zero whereas the DOD in cathode is raised up to about 0.82 at 2730 s. The zero SOC in anode indicates the end of the discharge process and the operation duration (i.e. 2730 s) indicates only about 75.8% of the stored electricity is discharged, meaning marginal loss at the cell capacity. The t_s -s are far more than the t_c -s and t_e as seen in Table 4, which means the lithium diffusion in the active materials cannot transport the

Time instant (s)	t_e (s)	t_s (s)		t_c (s)	
		Anode	Cathode	Anode	Cathode
5	173.5–189.5	2.6E3–2.7E3	71.1	13.2–23.2	5.5–7.6
10	169.3–202.4	2.0E3–2.4E3		11.5–33.8	3.8–5.7
50	149.6–274.2	432.4–1.1E3		15.2–38.1	0.2–1.6
100	152.6–272.8	165.8–419.8		10.4–45.1	0.1–1.7
120	150.0–272.1	132.9–337.9		14.9–46.7	0.1–1.5
160	144.3–296.7	113.8–236.9		18.1–40.1	0.1–1.1
185	142.7–417.5	102.8–175.6		16.7–31.2	0.0–0.9

Table 7. Time-variation of the t_e , t_s , and t_c during discharge for case 3.

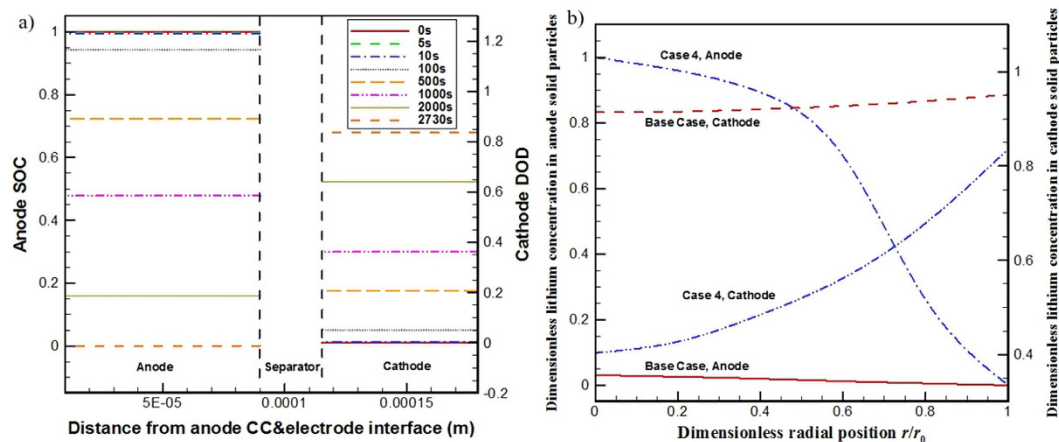


Figure 6. (a) Time-variation of the SOC in anode and the DOD in cathode for case 4, and (b) the lithium concentration in solid active particles at the end of discharge process for the base case and case 4.

lithium into the particle interior or out from the particle interior to the particle surface in time. It is the slow lithium diffusion speed in the solid active material particles that limits the cell discharge performance.

For case 4, the SOC in anode can be reduced down to zero, indicating seemingly that the cell can be fully discharged. We examined the lithium concentration in the solid active particles at the end of the discharge process, 2730 s. The simulated dimensionless lithium concentration distributions in both electrodes are displayed in Fig. 6(b). The displayed lithium concentration values are non-dimensionalized in terms of Eq. (19). Due to the too slow lithium diffusion speed in solid active materials, there exists large lithium concentration difference in the solid active material particles for both electrodes. At the end of discharge operation the dimensionless lithium concentration at the anode solid active particle surface is about 0, which is the minimum value it can reach, whereas it remains about 1 (i.e. unchanged from the beginning of the discharge process) at the center of the particle; in the cathode, the situation looks better, the dimensionless lithium concentration at the solid active material particle surface rises to about 0.8 while it is only about 0.4 at the center of the particle. It is the zero dimensionless lithium concentration at the solid anode active material particle surface that leads to the termination of the discharge process.

For comparison, the dimensionless lithium concentration distributions in solid active material particles at the end of the discharge process for the base case are also plotted in Fig. 6(b). Contrast to case 4, for the base case, very small differences of dimensionless lithium concentration are seen in the solid active material particle for both electrodes, indicating the lithium diffusion processes in solid active materials are fast enough and will not impose any limitations to the cell discharge performance.

Table 8 summarizes the time-variation of the t_e , t_s , and t_c for case 4. The t_s in anode decreases with time but is always larger the t_s in cathode; the t_e and t_c -s all slightly change with time due to the spatial and temporal changes of D_e , c_e and j^{Li} . However, the t_s -s in anode and cathode both are always at least one order of magnitude larger than the t_e and the corresponding t_c , meaning the cell performance is limited by the lithium diffusion processes in solid active materials. Moreover, as the t_s in cathode is relatively shorter than that in the anode, the termination of the discharge process is mainly due to the depletion of lithium in the near-surface region of anode solid active material particles. (Refer to Fig. 6(b))

Effects of charge transport. During charge/discharge of Li-ion batteries, the ionic charge is transporting in the electrolyte phase between the two electrodes across the separator and the electronic charge is transporting in the solid phase of electrodes. Theoretically, the ionic and electronic charge transports will always seek pathways

Time instant (s)	t_c (s)	t_s (s)		t_e (s)	
		Anode	Cathode	Anode	Cathode
10	180.1–180.2	5.0E4	1.1E3	155.2	94.3
100	180.3–180.5	3.6E4		163.3	87.1
500	180.3–180.5	1.1E4		163.3	87.1
1000	180.3–180.5	4.2E3		163.3	87.1
1800	180.3–180.5	1.9E3		163.3	87.1
2400	180.3–180.5	1.3E3		163.3	87.1
2730	180.3–180.5	1.1E3		163.3	87.1

Table 8. Time-variation of the t_s , t_e , and t_c during discharge for case 4.

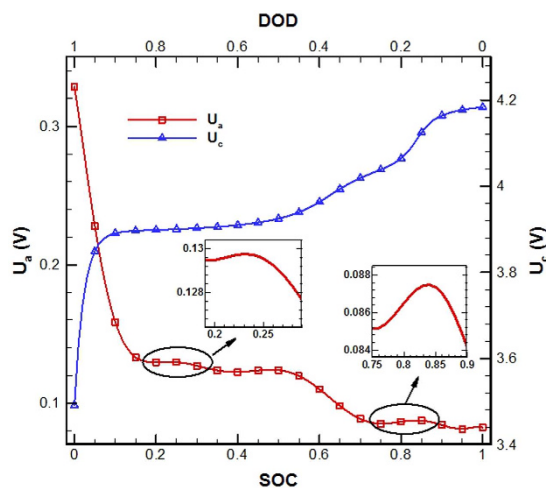


Figure 7. Open circuit potential of anode (Li_xC_6), U_a , and cathode ($\text{Li}_{1-x}\text{CoO}_2$), U_c .

of the least total resistance, which affects local EC reaction intensity (i.e. the magnitude of j^{Li}) in the anode and cathode electrodes. Qualitatively, if the R_e , defined by Eq. (11), is greater than the R_s , defined by Eq. (12), the EC reaction will tend to occur in the near-region of the separator for anode and cathode both to reduce the ionic charge transport resistance in the electrolyte, otherwise, it will tend to occur in the near-region of the current collector for anode and cathode both to reduce the electronic charge transport resistance in the electrodes. As the overpotential (η), which is the driving force of EC reactions, is linearly dependent on the open-circuit potential (U_a in anode or U_c in cathode), one other factor that affects or even dominates the EC reaction distribution in electrodes is the open-circuit potentials. The U_a is a function of the SOC in anode and the U_c is a function of the DOD in cathode, as defined by Eqs (17) and (18), respectively.

Seen from Tables 4 and 5, for the base case, the R_e in anode is about $4.9 \times 10^{-5} \Omega$, much larger than the R_s , $1.7 \times 10^{-6} \Omega$; the R_e in cathode is about $4.9 \times 10^{-5} \Omega$, larger than but still on the same order of magnitude of the R_s , $1.0 \times 10^{-5} \Omega$. The R_e and R_s are both very small and only lead to very small φ_s and φ_e differences, about a few millivolt φ_e difference through the cell, about 0.03 millivolt φ_s difference in the anode, and about 0.1 millivolt φ_s difference in the cathode (Refer to Fig. 3(c,d)). Figure 7 depicts the curves of open-circuit potential versus DOD in the cathode or SOC in the anode. When discharging, the U_c decreases with the increasing DOD and the U_a increases overall with the decreasing SOC though some fluctuations are seen. However, the locally magnified images in Fig. 7 clearly indicate that even the amplitudes of fluctuations at U_a are at least a few millivolts larger than the resultant φ_s and φ_e differences in the cell. Therefore, for the base case, the EC reactions should be dominated more by the spatial and temporal changes of U_a and U_c . This well explains the observations from Fig. 3(h), which presents the spatial and temporal evolution of j^{Li} in the two electrodes for the base case.

To further clarify the effects of charge transport on the cell charge/discharge performance, two more cases (cases 5 and 6) were simulated. Case 5 considers a 10-times reduced electric conductivity and case 6 a 100-times reduced electric conductivity compared with the base case. Figure 8(a) gives the obtained output cell voltage curves for the base case, case 5, and case 6, respectively. The three curves vary almost in the same trace; the locally magnified insets show that there exist small differences among them. The base case outputs the highest cell voltage, and case 6 the lowest, but the difference between them is very small, about 1 mV.

Figure 8(b) compares the j^{Li} profiles of the base case, case 5 and case 6 at three typical time instants: 0.1 s, 100 s and 1800 s. Increasing the R_e effectively adjusts the j^{Li} distribution in both electrodes; the EC reaction tends to more preferably occur in the near-region of the current collector for anode and cathode both.

For case 6, the R_e is $1.7 \times 10^{-4} \Omega$ in anode and $1.0 \times 10^{-3} \Omega$ in cathode, both 100 times larger than that for the base case. Figure 9 presents the simulated spatial and temporal evolution of j^{Li} in the two electrodes. Compared

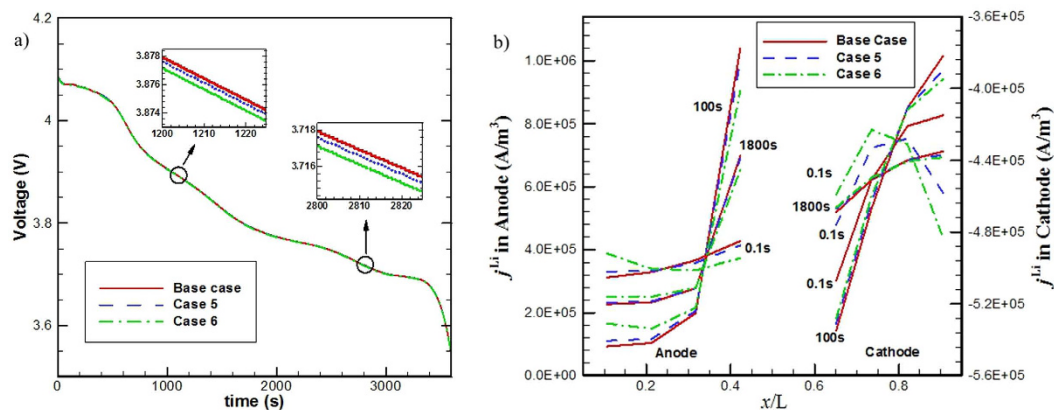


Figure 8. (a) Voltage curves of the base case, case 5 and case 6, and (b) comparison of j^{Li} profiles of the base case, case 5 and case 6 at three typical time instants.

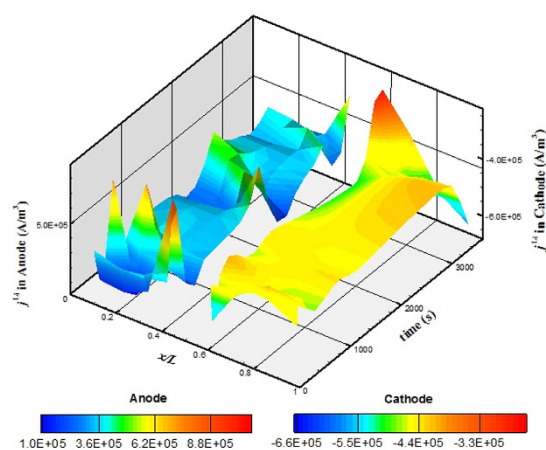


Figure 9. Spatial and temporal evolution of j^{Li} in the cell when discharging for case 6.

with Fig. 3(h), which displays the results from the base case, the j^{Li} in Fig. 9 shows qualitatively similar variation trends, but the variation range is about 15% narrower for both electrodes. The increased R_s 's make the EC reactions more uniformly occur in the electrodes.

Conclusions

To understand the mechanisms of Li-ion battery performance being limited by species and charge transport, the present work established a general characteristic parameter analysis method. Five parameters were proposed to characterize the involved species and charge transport during battery charge/discharge processes. The first three are characteristic time parameters, namely: (1) t_e , which characterizes the Li-ion transport rate in the electrolyte phase, (2) t_s , characterizing the lithium diffusion rate in the solid active materials, and (3) t_c , describing the local Li-ion depletion rate in electrolyte phase at the electrolyte/electrode interface due to EC reactions. The other two are electric resistances: R_c and R_s , which represent the equivalent ionic transport resistance and the effective electronic transport resistance in the electrode, respectively.

We then established a three-dimensional electrochemical model for the graphite/LiPF₆/LiCoO₂ battery and simulated its discharge processes with various battery designs or operational parameters, including thick and thin electrode design, high and low discharge rate, large and small active material particles in electrodes, and high and low electric conductivity in the solid phase. Carefully analyzing the simulation results corroborates that so long as the three characteristic time parameters are on the same order of magnitude, the battery may not get into any performance-limitations caused by the species transport processes. The simulation results unravel that the performance-limitation of thick electrode battery is essentially due to the too slow Li-ion species transport in-between the two electrodes across the separator and the performance-limitation of batteries at high-rate operations is essentially due to the very fast local depletion of Li-ions in the electrolyte at the interface of solid active materials and electrolyte by the EC reaction. The simulation results indicate as well that the battery with very large active material particles in electrodes may have too large t_s , making the battery performance limited by the too slow lithium diffusion from solid active material particle interior to its surface or the inverse.

The R_c and R_s are defined for both anode and cathode. Theoretically, the charge transports including the ionic and electronic charge transport will always seek transport paths of the least total transport resistance. That is to

say, the relative magnitude of R_c and R_s will affect the φ_s and φ_e distributions in the corresponding electrode. Numerical simulations reveal that increasing the relative magnitude of R_s to R_c makes the EC reaction tend to occur in the near-region of current collector for anode and cathode both, leading to more uniform EC reactions in the electrodes.

The characteristic parameter analysis method established in the present work may be applicable to or adaptable for use in other similar electrochemical systems that involve species and charge transports, such as the electrolyser, photoelectrochemical system, solar cell and various fuel cells. Caution must be paid to the different species transport mechanisms involved in different electrochemical systems. We take the H_2/O_2 proton exchange membrane fuel cell (PEMFC) as an example. The transport of reactants (i.e. H_2 and O_2) in PEMFC relies not only on molecular diffusion like the lithium species transport in solid active particles considered in the present work, but also on fluid convection, the characteristic time parameters that describe H_2 and O_2 transports must have different definitions to that for the lithium species transport in solid active particles in lithium-ion batteries. Future work may expend efforts on studying the transferability of the present method to other similar electrochemical systems.

References

1. Armand, M. The history of polymer electrolytes. *Solid State Ionics* **69**, 309–319 (1994).
2. Koksang, R., Olsen, I. I. & Shackle, D. Review of hybrid polymer electrolytes and rechargeable lithium batteries. *Solid State Ionics* **69**, 320–335 (1994).
3. Dunn, B., Kamath, H. & Tarascon, J.-M. Electrical energy storage for the grid: a battery of choices. *Science* **334**, 928–935 (2011).
4. Yang, P. & Tarascon, J.-M. Towards systems materials engineering. *Nature materials* **11**, 560–563 (2012).
5. Ramadesigan, V. *et al.* Modeling and simulation of lithium-ion batteries from a systems engineering perspective. *Journal of The Electrochemical Society* **159**, R31–R45 (2012).
6. Dahn, J., Fuller, E., Obrovac, M. & Von Sacken, U. Thermal stability of Li_xCoO_2 , Li_xNiO_2 and $\lambda-MnO_2$ and consequences for the safety of Li-ion cells. *Solid State Ionics* **69**, 265–270 (1994).
7. Thackeray, M. M. Manganese oxides for lithium batteries. *Progress in Solid State Chemistry* **25**, 1–71 (1997).
8. Padhi, A. K., Nanjundaswamy, K. & Goodenough, J. Phospho-olivines as positive-electrode materials for rechargeable lithium batteries. *Journal of the electrochemical society* **144**, 1188–1194 (1997).
9. Winter, M., Besenhard, J. O., Spahr, M. E. & Novak, P. Insertion electrode materials for rechargeable lithium batteries. *Advanced materials* **10**, 725–763 (1998).
10. Wang, H., Jang, Y. L., Huang, B., Sadoway, D. R. & Chiang, Y. M. TEM Study of Electrochemical Cycling-Induced Damage and Disorder in $LiCoO_2$ Cathodes for Rechargeable Lithium Batteries. *Journal of the Electrochemical Society* **146**, 473–480 (1999).
11. Huang, H., Yin, S.-C. & Nazar, L. s. Approaching theoretical capacity of $LiFePO_4$ at room temperature at high rates. *Electrochemical and Solid-State Letters* **4**, A170–A172 (2001).
12. Vazquez-Arenas, J., Gimenez, L. E., Fowler, M., Han, T. & Chen, S.-k. A rapid estimation and sensitivity analysis of parameters describing the behavior of commercial Li-ion batteries including thermal analysis. *Energy Conversion and Management* **87**, 472–482 (2014).
13. Zheng, H., Li, J., Song, X., Liu, G. & Battaglia, V. S. A comprehensive understanding of electrode thickness effects on the electrochemical performances of Li-ion battery cathodes. *Electrochimica Acta* **71**, 258–265 (2012).
14. Choi, J. *et al.* Effect of $LiCoO_2$ Cathode Density and Thickness on Electrochemical Performance of Lithium-Ion Batteries. *Journal of Electrochemical Science and Technology* **4**, 27–33 (2013).
15. Ye, J., Baumgaertel, A. C., Wang, Y. M., Biener, J. & Biener, M. M. Structural Optimization of 3D Porous Electrodes for High-Rate Performance Lithium Ion Batteries. *ACS nano* **9**, 2194–2202 (2014).
16. Jeong, J., Lee, H., Choi, J., Ryou, M.-H. & Lee, Y. M. Effect of $LiFePO_4$ cathode density and thickness on electrochemical performance of lithium metal polymer batteries prepared by *in situ* thermal polymerization. *Electrochimica Acta* **154**, 149–156, doi: 10.1016/j.electacta.2014.12.051 (2015).
17. Dimitrijevic, B., Aifantis, K. & Hackl, K. The influence of particle size and spacing on the fragmentation of nanocomposite anodes for Li batteries. *Journal of Power Sources* **206**, 343–348 (2012).
18. Xiao, L. *et al.* Influence of particle sizes and morphologies on the electrochemical performances of spinel $LiMn_2O_4$ cathode materials. *Journal of Power Sources* **225**, 286–292 (2013).
19. Xue, L. *et al.* Effect of particle size on rate capability and cyclic stability of $LiNi_{0.5}Mn_{1.5}O_4$ cathode for high-voltage lithium ion battery. *Journal of Solid State Electrochemistry* **19**, 569–576, doi: 10.1007/s10008-014-2635-4 (2014).
20. Wang, D. *et al.* The influence of the TiO_2 particle size on the properties of $Li_4Ti_5O_{12}$ anode material for lithium-ion battery. *Ceramics International* **40**, 3799–3804, doi: 10.1016/j.ceramint.2013.09.038 (2014).
21. Pohjalainen, E., Rauhala, T., Valkeapää, M., Kallioinen, J. & Kallio, T. Effect of $Li_4Ti_5O_{12}$ Particle Size on the Performance of Lithium Ion Battery Electrodes at High C-Rates and Low Temperatures. *The Journal of Physical Chemistry C* **119**, 2277–2283, doi: 10.1021/jp509428c (2015).
22. Li, J., Murphy, E., Winnick, J. & Kohl, P. Studies on the cycle life of commercial lithium ion batteries during rapid charge–discharge cycling. *Journal of Power Sources* **102**, 294–301 (2001).
23. Ning, G., Haran, B. & Popov, B. N. Capacity fade study of lithium-ion batteries cycled at high discharge rates. *Journal of Power Sources* **117**, 160–169 (2003).
24. Izumi, A. *et al.* Rapid charge and discharge property of high capacity lithium ion battery applying three-dimensionally patterned electrode. *Journal of Power Sources* **256**, 244–249 (2014).
25. Yuge, R., Tamura, N., Manako, T., Nakano, K. & Nakahara, K. High-rate charge/discharge properties of Li-ion battery using carbon-coated composites of graphites, vapor grown carbon fibers, and carbon nanohorns. *Journal of Power Sources* **266**, 471–474, doi: 10.1016/j.jpowsour.2014.05.068 (2014).
26. Wong, D., Shrestha, B., Wetz, D. A. & Heinzl, J. M. Impact of high rate discharge on the aging of lithium nickel cobalt aluminum oxide batteries. *Journal of Power Sources* **280**, 363–372, doi: 10.1016/j.jpowsour.2015.01.110 (2015).
27. Nagarajan, G. S., Van Zee, J. & Spotnitz, R. A Mathematical Model for Intercalation Electrode Behavior I. Effect of Particle-Size Distribution on Discharge Capacity. *Journal of the Electrochemical Society* **145**, 771–779 (1998).
28. Garcia, R. E., Chiang, Y.-M., Carter, W. C., Limthongkul, P. & Bishop, C. M. Microstructural modeling and design of rechargeable lithium-ion batteries. *Journal of The Electrochemical Society* **152**, A255–A263 (2005).
29. Golmon, S., Maute, K. & Dunn, M. L. A design optimization methodology for Li^+ batteries. *Journal of Power Sources* **253**, 239–250 (2014).
30. Du, W., Gupta, A., Zhang, X., Sastry, A. M. & Shyy, W. Effect of cycling rate, particle size and transport properties on lithium-ion cathode performance. *International Journal of Heat and Mass Transfer* **53**, 3552–3561 (2010).

31. Gupta, A. *et al.* Effective transport properties of LiMn_2O_4 electrode via particle-scale modeling. *Journal of The Electrochemical Society* **158**, A487–A497 (2011).
32. Du, W. *et al.* Optimization of LiMn_2O_4 electrode properties in a gradient-and surrogate-based framework. *Acta Mechanica Sinica* **29**, 335–347 (2013).
33. Xue, N. *et al.* Optimization of a single lithium-ion battery cell with a gradient-based algorithm. *Journal of The Electrochemical Society* **160**, A1071–A1078 (2013).
34. Du, W., Xue, N., Sastry, A. M., Martins, J. R. & Shyy, W. Energy density comparison of Li-ion cathode materials using dimensional analysis. *Journal of The Electrochemical Society* **160**, A1187–A1193 (2013).
35. Doyle, M., Newman, J., Gozdz, A. S., Schmutz, C. N. & Tarascon, J. M. Comparison of modeling predictions with experimental data from plastic lithium ion cells. *Journal of the Electrochemical Society* **143**, 1890–1903 (1996).
36. Doyle, M. & Newman, J. Analysis of capacity–rate data for lithium batteries using simplified models of the discharge process. *Journal of Applied Electrochemistry* **27**, 846–856 (1997).
37. Arora, P., Doyle, M., Gozdz, A. S., White, R. E. & Newman, J. Comparison between computer simulations and experimental data for high-rate discharges of plastic lithium-ion batteries. *Journal of power Sources* **88**, 219–231 (2000).
38. Smith, K. & Wang, C.-Y. Solid-state diffusion limitations on pulse operation of a lithium ion cell for hybrid electric vehicles. *Journal of Power Sources* **161**, 628–639 (2006).
39. Hasan, M. F., Chen, C. F., Shaffer, C. E. & Mukherjee, P. P. Analysis of the Implications of Rapid Charging on Lithium-Ion Battery Performance. *Journal of the Electrochemical Society* **162**, A1382–A1395, doi: 10.1149/2.0871507jes (2015).
40. Ogihara, N., Itou, Y., Sasaki, T. & Takeuchi, Y. Impedance Spectroscopy Characterization of Porous Electrodes under Different Electrode Thickness Using a Symmetric Cell for High-Performance Lithium-Ion Batteries. *The Journal of Physical Chemistry C* **119**, 4612–4619, doi: 10.1021/jp512564f (2015).
41. Zhao, R., Liu, J. & Gu, J. The effects of electrode thickness on the electrochemical and thermal characteristics of lithium ion battery. *Applied Energy* **139**, 220–229, doi: 10.1016/j.apenergy.2014.11.051 (2015).
42. Jiang, F., Peng, P. & Sun, Y. Thermal analyses of LiFePO_4 /graphite battery discharge processes. *Journal of Power Sources* **243**, 181–194 (2013).
43. Yang, S. & Tao, W. *Heat Transfer*. Vol. 1 (Beijing: Higher Education Press, 2006).
44. Wang, C.-Y. Fundamental models for fuel cell engineering. *Chemical reviews* **104**, 4727–4766 (2004).
45. Andersson, M., Yuan, J. & Sundén, B. Review on modeling development for multiscale chemical reactions coupled transport phenomena in solid oxide fuel cells. *Applied Energy* **87**, 1461–1476, doi: 10.1016/j.apenergy.2009.11.013 (2010).
46. Zhang, X. & Bieberle-Hutter, A. Modeling and Simulations in Photoelectrochemical Water Oxidation: From Single Level to Multiscale Modeling. *ChemSusChem* **9**, 1223–1242, doi: 10.1002/cssc.201600214 (2016).
47. Wang, C., Gu, W. & Liaw, B. Micro-Macroscopic Coupled Modeling of Batteries and Fuel Cells I. Model Development. *Journal of the Electrochemical Society* **145**, 3407–3417 (1998).
48. Doyle, M., Fuller, T. F. & Newman, J. Modeling of galvanostatic charge and discharge of the lithium/polymer/insertion cell. *Journal of the Electrochemical Society* **140**, 1526–1533 (1993).
49. Fuller, T. F., Doyle, M. & Newman, J. Simulation and optimization of the dual lithium ion insertion cell. *Journal of the Electrochemical Society* **141**, 1–10 (1994).
50. Chung, D. W., Ebner, M., Ely, D. R., Wood, V. & Garcia, R. E. Validity of the Bruggeman relation for porous electrodes. *Model. Simul. Mater. Sci. Eng.* **21**, 16, doi: 10.1088/0965-0393/21/7/074009 (2013).
51. Jiang, F., Oliveira, M. S. A. & Sousa, A. C. M. Mesoscale SPH modeling of fluid flow in isotropic porous media. *Computer Physics Communications* **176**, 471–480, doi: http://dx.doi.org/10.1016/j.cpc.2006.12.003 (2007).
52. Gao, K., Dai, C.-S., Lv, J. & Feng, X.-M. Effects of carbon contents on morphology and electrical properties of $\text{Li}_2\text{MnSiO}_4/\text{C}$ prepared by a vacuum solid-state method. *Russian Journal of Electrochemistry* **50**, 267–273, doi: 10.1134/s1023193513050066 (2013).
53. Sun, X. F. *et al.* Triple-Cation-Doped $\text{Li}_3\text{V}_2(\text{PO}_4)_3$ Cathode Material for Lithium Ion Batteries. *Acta Phys.-Chim. Sin.* **31**, 1513–1520, doi: 10.3866/pku.whxb201506082 (2015).
54. Lyu, Z. Y. *et al.* Nitrogen-Doped Carbon Nanocages as High-Rate Anode for Lithium Ion Batteries. *Acta Chim. Sin.* **73**, 1013–1017, doi: 10.6023/a15040289 (2015).
55. Fang, L., Zhang, H. J., Zhang, Y., Liu, L. & Wang, Y. Design and synthesis of two-dimensional porous Fe-doped LiCoPO_4 nano-plates as improved cathode for lithium ion batteries. *Journal of Power Sources* **312**, 101–108, doi: 10.1016/j.jpowsour.2016.02.035 (2016).
56. Fang, W., Ramadass, P. & Zhang, Z. J. Study of internal short in a Li-ion cell-II. Numerical investigation using a 3D electrochemical-thermal model. *Journal of Power Sources* **248**, 1090–1098 (2014).
57. Somasundaram, K., Birgersson, E. & Mujumdar, A. S. Thermal–electrochemical model for passive thermal management of a spiral-wound lithium-ion battery. *Journal of Power Sources* **203**, 84–96 (2012).
58. Valoen, L. O. & Reimers, J. N. Transport properties of LiPF_6 -based Li-ion battery electrolytes. *Journal of The Electrochemical Society* **152**, A882–A891 (2005).
59. Fang, W., Kwon, O. J. & Wang, C. Y. Electrochemical–thermal modeling of automotive Li-ion batteries and experimental validation using a three-electrode cell. *International journal of energy research* **34**, 107–115 (2010).
60. Moggia, E. & Bianco, B. Mean activity coefficient of electrolyte solutions. *The Journal of Physical Chemistry B* **111**, 3183–3191 (2007).

Acknowledgements

Financial support received from the Key Scientific Development Project of Guangdong Province (2015A030308019), the Guangzhou Scientific and Technological Development Plan (2014J4100217), the Guangdong Key Laboratory of New and Renewable Energy Research and Development Fund (Y607jg1001) and the CAS “100 talents” Program (FJ) is gratefully acknowledged.

Author Contributions

F.J. proposed the main idea and wrote about 2/3 of the paper. P.P. performed the simulations, prepared all the figures, and wrote about 1/3 of the paper. Both the authors reviewed the manuscript.

Additional Information

Competing financial interests: The authors declare no competing financial interests.

How to cite this article: Jiang, F. and Peng, P. Elucidating the Performance Limitations of Lithium-ion Batteries due to Species and Charge Transport through Five Characteristic Parameters. *Sci. Rep.* **6**, 32639; doi: 10.1038/srep32639 (2016).



This work is licensed under a Creative Commons Attribution 4.0 International License. The images or other third party material in this article are included in the article's Creative Commons license, unless indicated otherwise in the credit line; if the material is not included under the Creative Commons license, users will need to obtain permission from the license holder to reproduce the material. To view a copy of this license, visit <http://creativecommons.org/licenses/by/4.0/>

© The Author(s) 2016